

RECEIVED: October 13, 2023



















REVISED: December 10, 2023

ACCEPTED: December 29, 2023

PUBLISHED: February 5, 2024

24<sup>TH</sup> INTERNATIONAL WORKSHOP ON RADIATION IMAGING DETECTORS  
OSLO, NORWAY  
25–29 JUNE 2023

## A two-layer Timepix3 stack for improved charged particle tracking and radiation field decomposition

P. Smolyanskiy <sup>a,\*</sup> M. Bacak <sup>b</sup> B. Bergmann <sup>a</sup> P. Broulím <sup>c</sup> P. Burian <sup>a,c</sup>  
T. Čelko <sup>a,d</sup> D. Garvey <sup>a</sup> K. Gunthoti <sup>e</sup> F.G. Infantes <sup>f,b</sup> P. Mánek <sup>a,g</sup> A. Manna <sup>h,i</sup>  
F. Mráz <sup>d</sup> R. Mucciola <sup>j,k</sup> S. Pospíšil <sup>a</sup> M. Sitarz <sup>l</sup> O. Urban <sup>c</sup> Z. Vykydal <sup>m</sup>  
and S.A. Wender <sup>e</sup>

<sup>a</sup>*Institute of Experimental and Applied Physics, Czech Technical University in Prague,  
Husova 240/5, Prague, Czech Republic*

<sup>b</sup>*CERN,  
Espl. des Particules 1, Geneva, Switzerland*

<sup>c</sup>*Faculty of Electrical Engineering of the University of West Bohemia,  
Univerzitní 26, Pilsen, Czech Republic*

<sup>d</sup>*Department of Software and Computer Science Education, Charles University,  
Malostranské nám. 2/25, Prague, Czech Republic*

<sup>e</sup>*Los Alamos Neutron Science Center, Los Alamos National Laboratory,  
P.O. Box 1663, Los Alamos, U.S.A.*

<sup>f</sup>*University of Granada,  
Avenida del Hospicio 1, Granada, Spain*

<sup>g</sup>*Department of Physics and Astronomy, University College London,  
Gower St., London, United Kingdom*

<sup>h</sup>*University of Bologna,  
Via Zamboni 33, Bologna, Italy*

<sup>i</sup>*INFN, Bologna Section,  
Viale Berti Pichat 6/2, Bologna, Italy*

<sup>j</sup>*University of Turin,  
Via Giuseppe Verdi 8, Torino, Italy*

<sup>k</sup>*INFN, Turin Section,  
Via Pietro Giuria 1, Torino, Italy*

<sup>l</sup>*Danish Centre for Particle Therapy, Aarhus University Hospital,  
Palle Juul-Jensens Boulevard 99, Aarhus, Denmark*

<sup>m</sup>*Czech Metrology Institute,  
Okružní 31, Brno, Czech Republic*

E-mail: [petr.smolyanskiy@cvut.cz](mailto:petr.smolyanskiy@cvut.cz)

\*Corresponding author.

**ABSTRACT:** We characterize a novel instrument designed for radiation field decomposition and particle trajectory reconstruction for application in harsh radiation environments. The device consists of two Timepix3 assemblies with 500  $\mu\text{m}$  thick silicon sensors in a face-to-face geometry. These detectors are interleaved with a set of neutron converters:  ${}^6\text{LiF}$  for thermal neutrons, polyethylene (PE) for fast neutrons above 1 MeV, and PE with an additional aluminum recoil proton filter for neutrons above  $\sim 4$  MeV. Application of the coincidence and anticoincidence technique together with pattern recognition allows improved separation of charged and neutral particles, their discrimination against  $\gamma$ -rays and assessment of the overall directionality of the fast neutron field. The instrument's charged particle tracking and separation capabilities were studied at the Danish Center for Particle Therapy (DCPT), the Proton Synchrotron, and Super Proton Synchrotron with protons (50–240 MeV), pions (1–10 GeV/c and 180 GeV/c). After developing temporal and spatial coincidence assignment methodology, we determine the relative amount of coincident detections as a function of the impact angle, present the device's impact angle resolving power (both in coincidence and anticoincidence channels). The detector response to neutrons was studied at the Czech Metrology Institute (CMI), at n-ToF and the Los Alamos Neutron Science Center (LANSCE), covering the entire spectrum from thermal up to 600 MeV. The measured tracks were assigned to their corresponding neutron energy by application of the time of flight technique. We present the achieved neutron detection efficiency as a function of neutron kinetic energy and demonstrate how the ratio of events found below the different converters can be used to assess the hardness of the neutron spectrum. As an application, we determine the neutron content within a PMMA phantom just behind the Bragg-peak during clinical irradiation condition with protons of 160 MeV.

**KEYWORDS:** Neutron detectors (cold, thermal, fast neutrons); Particle identification methods; Particle tracking detectors (Solid-state detectors)

---

## Contents

<b>1</b>	<b>Introduction</b>	<b>1</b>
<b>2</b>	<b>Materials and methods</b>	<b>1</b>
2.1	Detector design	1
2.2	Experimental setups	2
2.3	Data analysis	3
2.4	Allpix Squared simulation	4
<b>3</b>	<b>Results</b>	<b>4</b>
3.1	Coincidence and anticoincidence techniques	4
3.2	Particle tracking — angle resolving power	4
3.3	Neutron calibration results	5
3.4	Mixed field: measurement of the neutron fluxes within a PMMA phantom behind the Bragg-peak during irradiation with protons	8
<b>4</b>	<b>Conclusions and outlook</b>	<b>8</b>

---

## 1 Introduction

Precise measurement of radiation levels and radiation field characteristics is a major concern in fundamental physics, life-science applications, for safety around nuclear facilities or in nuclear medicine. For example, Medipix2 [1] and Timepix [2] detector networks installed in ATLAS have been employed to measure the radiation levels and radiation field composition during and in between collision periods [3–5]. The information provided by these radiation monitors has significantly contributed to precise luminosity determination [6, 7] and benchmarking of simulations [8]. The latter are crucial for defining the radiation hardness of detector systems, while helping in understanding radiation induced effects in the used electronics at different locations within ATLAS. The addition of Timepix3 detectors towards the end of Run-2 has provided data with 1.6 ns time stamping of particle traces, allowing to resolve individual LHC bunches in (quasi-)dead time free measurements independent of the ATLAS trigger scheme [9, 10]. The Timepix3 single-layer particle tracking capability has been demonstrated within MoEDAL, where Timepix3 was placed at a distance of  $\sim 1$  m (on top of the LHCb Velo dust cover) with a relatively unobstructed view to IP8 [11]. Based on these operational experiences, we propose a novel two-layer Timepix3 design, improving not only the capability to separate the charged and neutral component of the radiation fields but also the particle trajectory reconstruction, in particular, at close to perpendicular particle impact.

## 2 Materials and methods

### 2.1 Detector design

The proposed detector consists of two Timepix3 [12] chips bump-bonded to 500  $\mu\text{m}$  thick silicon sensors (figure 1). Timepix3 is a pixelated readout chip developed within the Medipix3 collaboration [13]. It

provides a 1.6 ns time binning, data-driven readout, and simultaneous measurement of energy and time in each of its  $256 \times 256$  pixels, with a  $55 \mu\text{m}$  pitch. The sensor layers face each other with a set of thermal and fast neutron converters in between (figure 1). The two-layer design allows for the separation of penetrating charged particles from neutrons using coincidence and anticoincidence information, and for the determination of the directionality of the fast neutron field (a fast neutron will be seen on either of the layers). Moreover, it allows an improved (in comparison with a single layer detector) calculation of impact angles close to the sensor normal. The converters divide the area of each sensor into four quadrants. The first region located behind  $\sim 1$  mm thick polyethylene (marked as PE in figure 1) layer serves the purpose of detecting recoil protons generated from fast neutron interactions with the hydrogen-rich material. Introducing an  $80 \mu\text{m}$  thick aluminum proton-stopping filter beneath one half of the PE layer (region PE+Al) reduces the quantity of low-energy recoil protons reaching the sensor's surface, thus providing region with differing fast neutron sensitivity up to  $\sim 20$  MeV. The third region is covered by a  ${}^6\text{LiF}$  foil with a thickness of  $5 \text{ mg/cm}^2$  ( ${}^6\text{Li}$  enrichment of 89 %), possessing a substantial cross-section (940 b) for capturing thermal neutrons. Consequently, thermal neutrons are detected through the emission of  $\alpha$ -particles and tritons. An uncovered region, referred to as Si, is designated for subtraction of the events created by neutron interactions in silicon and the non-neutron field.

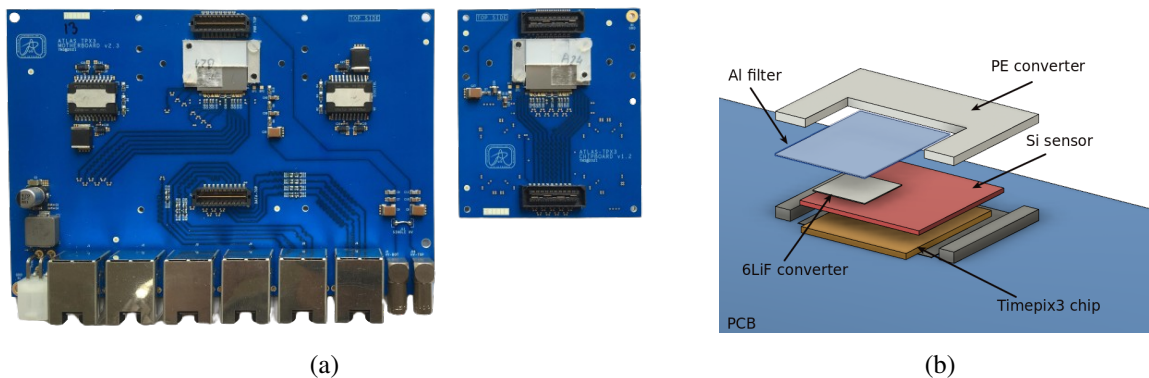


**Figure 1.** (a) Photograph of the two-layer Timepix3 detector: the motherboard (right) and daughterboard (left). (b) Exploded view of the Timepix3 detector assembly with neutron converters.

Per-pixel energy calibration of the device was conducted with X-ray fluorescences and characteristic  $\gamma$ -rays as described in [14]. The threshold was conservatively set at 5 keV for both layers. For device control, read out, and sensor biasing, a customized Katherine readout interface [15] was used. It was designed for operation at long distances from the detector (maximum of 20 m with maximum speed of 80 Mpix/s). Throughout the present work, a bias voltage of 200 V was applied to both sensors. The temperature of the sensors and chips during the operation and calibration was around  $50^\circ\text{C}$ .

## 2.2 Experimental setups

A first measurement was done within an isotropic thermal neutron field at the Czech Metrology Institute (CMI) created by moderating fast neutrons from Pu-Be source in a graphite pile [16, 17]. The fast neutron response was studied at the Weapons Neutron Research (WNR) facility of the Los Alamos Neutron Science Center (LANSCE) [18]. The detector was positioned at a distance of 20.6 m from the interaction point at Flight Path 30L. Neutrons are generated through a spallation reaction when an 800 MeV LINAC proton beam strikes a cylindrical tungsten target. To ensure the purity of

the neutron signal, any charged particles remaining in the beam are removed using a magnetic field. The proton beam is divided into macropulses with a duration of 625  $\mu\text{s}$ , operating at a repetition rate of 100 Hz. Each macropulse contains 347 distinct micropulses, characterized by a full width at half maximum (FWHM) of approximately 125 picoseconds, and these micropulses are separated by 1.8  $\mu\text{s}$ . To extend the measured device response towards thermal neutron region the testbeam campaign was carried out at the NEL (neutron escape line) of the n\_TOF facility at CERN [19, 20]. The detector was installed at a distance of 185 m to the interaction point where 20 GeV/c protons impinge on a massive Pb block surrounded by a water layer acting as moderator. To investigate the detector's response to (quasi-)monoenergetic neutron impacts, the time-of-flight (ToF) technique as described in [21] was utilized in the latter two experiments.

The charged particle response was determined in experiments at the Proton Synchrotron (PS) and the Super Proton Synchrotron (SPS) in hadron beams (90% pion content) of 1, 10, 15 GeV/c and 180 GeV/c, respectively. In all these experiments, the detector was rotated in the beam, and its response was analyzed at different impact angles with respect to the sensor normal. The response to protons of 80, 160 and 240 MeV protons was studied at the Danish Center for Particle Physics (DCPT) at the Aarhus hospital.

### 2.3 Data analysis

Timepix3 provides a stream of pixels triggered by particle interaction in the sensor. Using temporal (time window of 200 ns) and spatial (8-fold neighborhood) conditions, individual tracks (or clusters) of particles are identified in the stream of pixel hits separately for each layer. Each track is then sorted into one of the six basic cluster categories defined in [22]: dots, small blobs, curly tracks, straight tracks, heavy blobs, and heavy tracks. Moreover, for each measured track the impact angles and  $dE/dX$  are determined as described in [23]. In the case that within the coincidence time window clusters are present in both layers, we further evaluate whether these tracks are caused by the same particle (coincidence). Therefore, based on the impact angle determination, the particle trajectory is extrapolated towards the other layer. If the energy weighted center of the track on the opposing layer lies within a circle with radius  $r_{\text{coinc}} = 10$  around the intersection point, we label the event as a coincidence detection.

For neutron detection through converters, only anticoincident high energy transfer events (HETE) were considered. These correspond to products of the nuclear reaction of neutrons with converter material (recoil protons,  $\alpha$ -particles, and tritons). HETE are seen as “heavy tracks” (large elliptical traces) and “heavy blobs” (large round traces). As shown in previous works [26, 27], this provides excellent separation from  $\gamma$ -rays. The efficiency of each neutron converter  $\varepsilon_i$  was calculated as

$$\varepsilon_i = \frac{N_i - \frac{A_i}{A_{\text{Si}}} N_{\text{Si}}}{\phi_{\text{source}} t}, \quad (2.1)$$

where  $N_i$  and  $N_{\text{Si}}$  are numbers of anticoincident HETE registered below the corresponding converter (PE, PE+Al,  ${}^6\text{LiF}$ ) and uncovered region of the sensor, respectively;  $A_i$  and  $A_{\text{Si}}$  are areas of each of converters and uncovered region of the detector, respectively;  $\phi_{\text{source}}$  is a reference flux provided by the radiation facility;  $t$  is a time of irradiation. Moreover, we assess the ratio of the response below PE and PE+Al as:

$$R_{\text{PE/PE+Al}} = \frac{\Delta N_{\text{PE}}}{\Delta N_{\text{PE+Al}}}, \quad (2.2)$$

where  $\Delta N_i = N_i - N_{\text{Si}} \frac{A_i}{A_{\text{Si}}}$  is the excess signal below the corresponding converters.

## 2.4 Allpix Squared simulation

To understand the device’s capabilities and performance, the device response to neutrons was simulated in the Allpix Squared framework [28], which is an open-source tool for Monte-Carlo simulation of silicon detectors. The device’s CAD model (including the aluminum box, PCBs, neutron converters, stopping foils and aluminum supports below the chips) was translated to GDML using the MRADSIM converter [29] and imported into Allpix Squared. Neutrons were emitted perpendicularly to the surface of the detector. Different physics lists were used for thermal (“Shielding”) and fast neutrons (“FTFP\_BERT\_LIV”). Two different propagation modules were applied for the charge carriers propagation through the sensor. To get the information about converter efficiencies and stopping foil effect, the *GenericPropagation* module was chosen. It provides fast simulation speed and accurate results. In such a case, there is no information about transient currents on pixels. Thus, it is not possible to obtain the full shape of the clusters and their proper energy spectrum. Clusters corresponding to the products of neutron reactions with converters were separated by the *cluster height* attribute (maximal energy deposition per cluster). Translation from the induced on pixel charges to the ADC counts was done by the *DefaultDigitizer* module. For accurate simulation of the recoiled protons energy spectrum, the *TransientPropagation* module was applied, while an in-house developed digitizer module was used properly describing the Timepix3 front-end electronics’ response.

## 3 Results

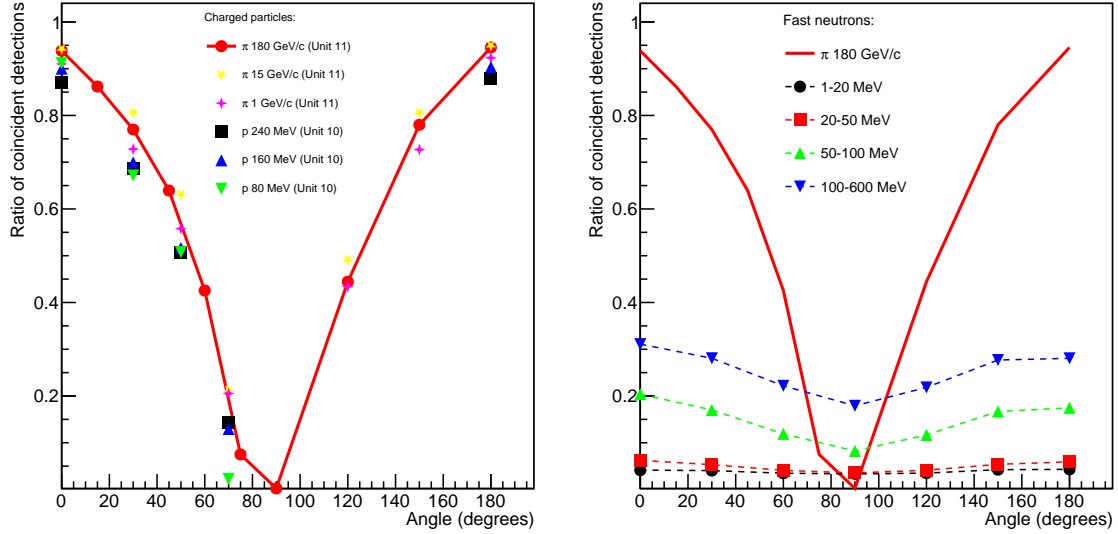
### 3.1 Coincidence and anticoincidence techniques

Figure 2 illustrates the angular dependence of the coincidence behavior for various particle types. The probability of simultaneously detecting charged particles, possessing sufficient energy to penetrate through both sensors, is influenced by the device’s geometry and the angle at which they impact. When the impact angle is 0 degrees (perpendicular), a charged particle detected in the first layer is automatically registered in the second layer, resulting in an almost 100% coincident detection rate. However, as the device is rotated within the beam, the effective detection area for particles exhibiting coincident behavior in both sensors gradually changes. At an impact angle of 90 degrees (parallel to the sensor surface), one would expect a purely anticoincident detection scenario.

Contrary to charged particles, neutrons interact randomly with the device. They either undergo interactions within one of the converter layers or within the silicon sensor. Therefore, a pure anticoincidence behavior is expected (see figure 2 below  $\sim 20\text{--}30$  MeV). At higher energies neutron-induced nuclear reactions within the first layer (or in air before the detector) can result in penetrating secondaries creating coincident events.

### 3.2 Particle tracking — angle resolving power

A two-layer device design allows for improved angle determination of charged particles, especially at impact angles close to sensor normal. In the following, we estimate the achievable angular resolution of the device as a function of the impact angle by determining the reconstructed angle spectra in both the coincidence and the anticoincidence channels for the 180 GeV/c pion beam. The peaks therein are then fitted with gaussian curves, whose means and widths are plotted against the “true” angles in figure 3. Particles crossing the edges of either of the sensors were excluded from the analysis.



**Figure 2.** Relative amount of coincident events as a function of the impact angle: (left) for the measurement in the charged particle beams; (right) for neutrons within different energy ranges.

Overall, a linear response was found with an ambiguity for angles above 90 degrees in both channels (figure 3(a)): it is not possible to determine the direction of flight. The angular resolution was found to be almost independent of the angle in the coincidence channel with an average resolution of  $\sigma = 0.28$  degrees, while the angle reconstruction in the anticoincidence channel strongly depends on the number of pixels available for angle determination and it is thus better at large impact angles (figure 3(b)).

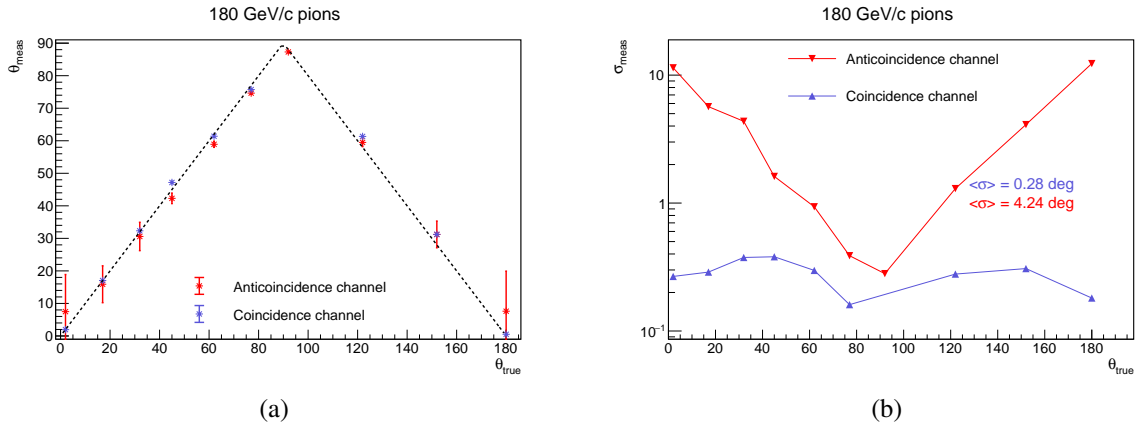


**Figure 3.** (a) Scatter plot of the reconstructed versus “true” angle extracted from the 180 GeV/c pion data set. The assigned errorbars depict the resolution; (b) Angular resolution as a function of the “true” angle.

### 3.3 Neutron calibration results

The neutron detection efficiency was determined according to eq. (2.2) from the neutron measurements at 0 degree. It is shown as a function of the neutron energy in figure 4. The measured efficiency is compared with simulation (at several energies) finding a decent agreement.

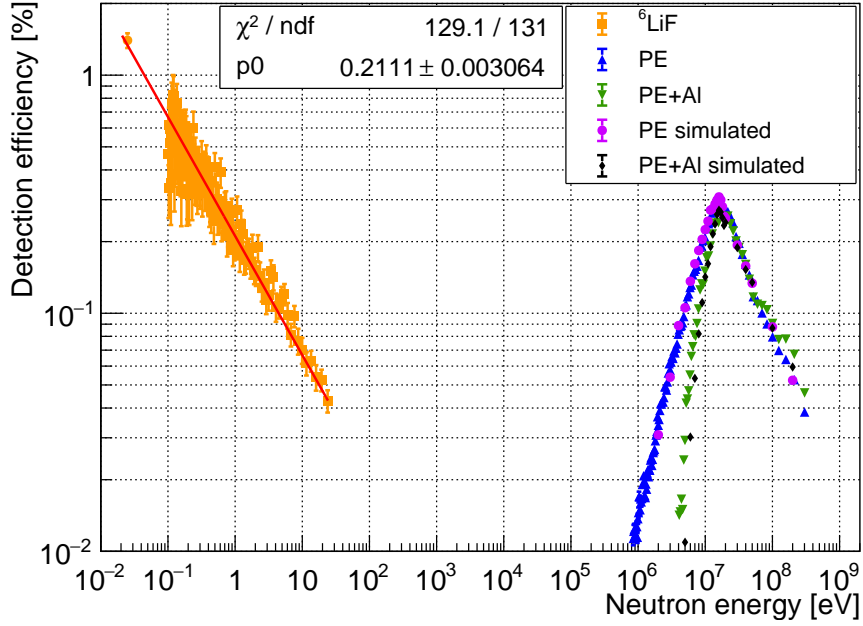


**Figure 4.** Measured neutron converter efficiencies as a function of neutron energy for the entire investigated energy range (thermal to 600 MeV). Fast neutrons were impacting at 0 degree. The obtained efficiencies are compared with simulation at discrete points. The  ${}^6\text{LiF}$  response was fitted with  $\varepsilon_{\text{LiF}} = \frac{p_0}{\sqrt{E_n}}$ .

The energy dependent efficiency of the  ${}^6\text{LiF}$  was determined from the CMI (at 25 meV) and the n\_ToF data (epithermal region). It decreases with energy as  $\varepsilon \sim \frac{1}{\sqrt{E_n}}$ , with an efficiency  $\varepsilon_{\text{thermal}} = 1.4\%$ . Since the products of the  ${}^6\text{Li}(n,\alpha){}^3\text{H}$ -reaction are emitted back to back, either the triton (emitted at 2.73 MeV) or the  $\alpha$ -particle (emitted at 2.05 MeV) is detected. While self-absorption in the converter, energy loss in the backside contact (dead layer) creates tails towards lower energy in the energy deposition spectrum, saturation of the pixel electronics at  $\sim 450$  keV results in an underestimation of the expected energies (see blue spectrum at figure 5).

The LANSCE data were used for assessment of the conversion efficiencies in the PE and PE+Al regions. An increased response below the PE layer becomes visible above a neutron energy of 1 MeV. The additionally inserted aluminum foil between the PE and the sensor in the PE+Al region effectively blocks recoil protons at neutron impact below 4 MeV. With increasing neutron energy the range of recoil protons increases, so that the efficiently used thickness of the converter increases. At higher energy, however, the recoils receiving a large energy from the neutrons become penetrating, leaving only part of their energy in the silicon sensor until eventually, the energy is not enough to create the required neutron signature of a HETE. Thus, a maximal efficiency  $\varepsilon_{\text{fast}}^{\text{max}} = 0.3\%$  was found at  $\sim 16$  MeV. Figure 5 shown the energy spectra of recoil protons at different incident neutron energies. Up to  $\sim 10$  MeV neutron energy, recoil protons are completely stopped in the sensor. Thus, the high energy edge relates to the recoil protons receiving the full energy of the neutron, which are affected by the saturation of the pixel electronics. Addition of the aluminum stopping foil reduces the observable maximal energy deposition by the energy loss in the foil. Towards higher neutron energy, the energetic recoil protons have sufficient energy to leave the sensor. Thus, the most energetic recoils leave only a fraction of their energy in the sensor creating peaks in the spectra with tails towards higher energy. The observed peak position are moving towards lower energies with increasing neutron energy.



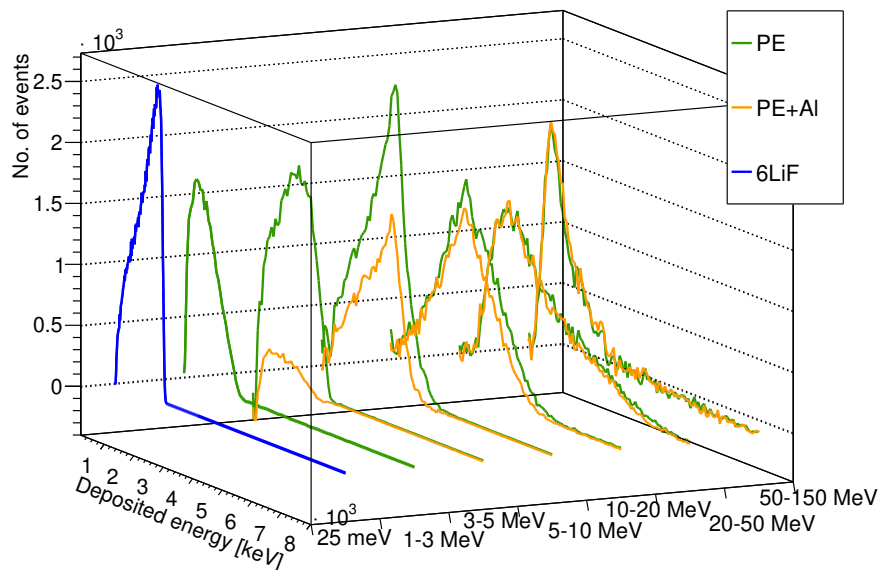


**Figure 5.** Energy deposition spectra of the neutron excess signals at different neutron energy: blue spectrum is seen below <sup>6</sup>LiF for the thermal neutron measurement at CMI. The spectrum is comprised of  $\alpha$ -particles (emitted at 2.05 MeV) and tritons (emitted at 2.73 MeV). Green and orange spectra are seen below the PE and the PE+Al region in different fast neutron energy regions measured at LANSCE. The spectra are comprised of the energy left by recoil protons in the sensor; the presented spectra are affected by energy losses in the converters itself, the backside contact including the dead layer of the sensor, as well as pixel electronics saturation.

Figure 6 shows the ratio of the excess signal in the PE and PE+Al regions  $R_{PE/PE+Al}$  as a function of the neutron energy. It is monotonically decreasing and flattens out at approximately 20 MeV neutron energy.

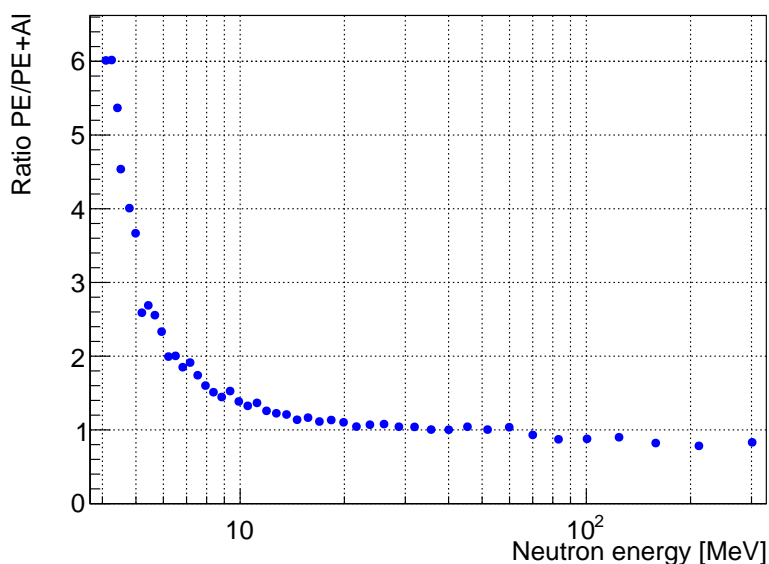


**Figure 6.** Ratio of the response below PE and PE+Al versus neutron energy.

### 3.4 Mixed field: measurement of the neutron fluxes within a PMMA phantom behind the Bragg-peak during irradiation with protons

To create a field of unknown composition, the detector was placed within a phantom built with PMMA blocks. The overall PMMA thickness in front of the detector was 45 cm, while 30 cm PMMA were downstream just behind the device. 160 MeV protons were shot into the PMMA blocks and are absorbed before they can reach the detector. A picture of the measurement setup is shown in figure 7(a).

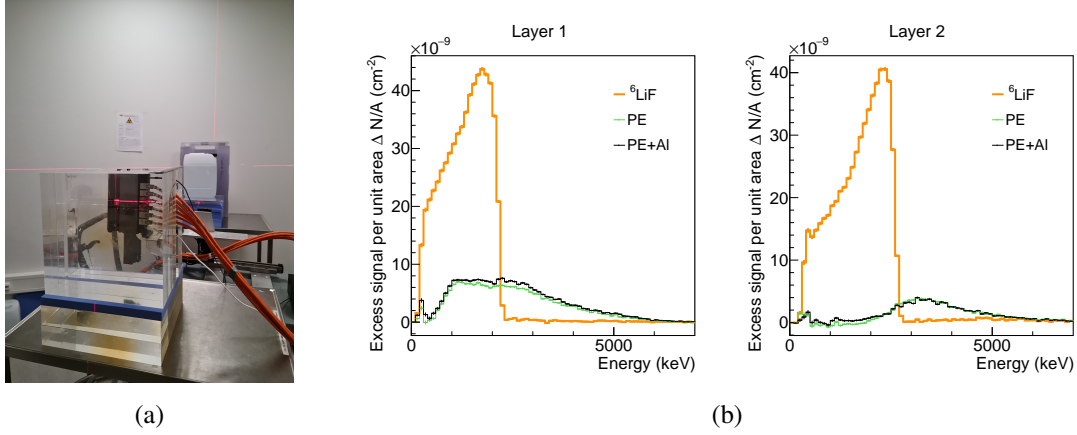


**Figure 7.** (a) Experimental setup; measurement within a phantom built from 15 cm thick PMMA blocks. The detector is surrounded by 45 cm PMMA upstream and 30 cm downstream. The proton beam energy was set at 160 MeV; (b) Measured excess energy signals below the different converters.

Table 1 gives the excess anticoincidence signals of the neutron-like events below the different converters in each layer of the device, integrated over the entire 30 minutes measurement duration. Enhanced responses are seen below all neutron converters. The ratio of events below the PE and PE+Al converters is  $1.16 \pm 0.01$  and  $1.06 \pm 0.03$  for layer 1 and layer 2, respectively. Together with the spectrum of recoil protons (figure 7(b)), we conclude that layer 1 detects fast neutrons with a mean neutron energy within the 5–20 MeV range, while layer 2 detects neutrons at a mean energy within the 20–100 MeV range. The amount of thermal neutrons detected by the two layers is similar. We determine the neutron flux rate as

$$\frac{dN_i}{dt} = \frac{\Delta N_i}{\varepsilon_i \times t_{\text{bin}}}, \quad (3.1)$$

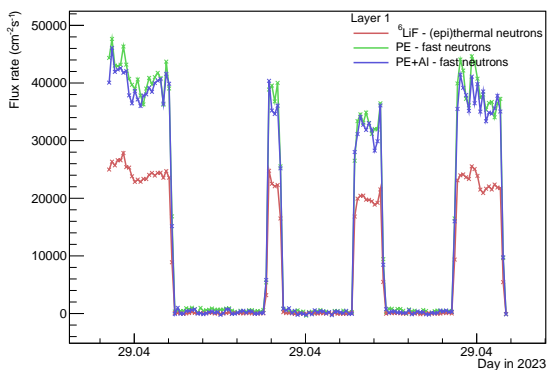
where the following detection efficiencies were extracted from the calibration measurement (figure 4):  $\varepsilon_{\text{PE}}^{\text{layer 1}} = 0.30\%$ ,  $\varepsilon_{\text{PE}}^{\text{layer 2}} = 0.13\%$ ,  $\varepsilon_{\text{PE+Al}}^{\text{layer 1}} = 0.27\%$ ,  $\varepsilon_{\text{PE+Al}}^{\text{layer 2}} = 0.13\%$ , and  $\varepsilon_{\text{LiF}} = 1.4\%$ . The determined neutron flux rates are shown as a function of measurement time in figure 8. We assess the overall uncertainty due to the incident energy determination and unknown impact angle to be 20%.

## 4 Conclusions and outlook

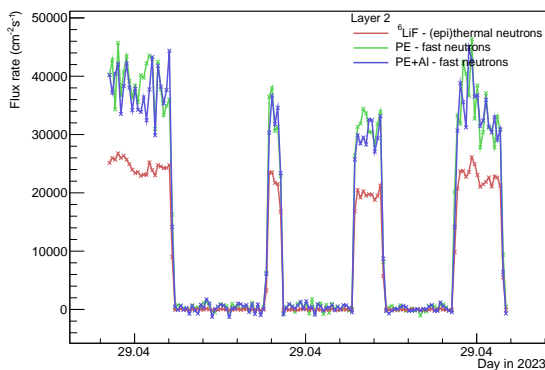
A two-layer Timepix3 detection setup improves particle tracking, neutron detection, and separation of neutral from charged particles. The capabilities of the anticoincidence and coincidence technique were evaluated with various charged particle species and neutrons of different energies. The neutron detection efficiencies of  ${}^6\text{LiF}$ , PE and PE+Al converters were calibrated in the energy range from

**Table 1.** Excess counts  $\Delta N_i = N_i - N_{\text{si}} \frac{A_i}{A_{\text{Si}}}$  measured below the converters and the ratio of the excess below the PE and PE+Al for the measurement within a PMMA phantom.

	layer 1	layer 2
$\Delta N_{\text{PE}}$	$112482 \pm 893$	$4463 \pm 885$
$\Delta N_{\text{PE+Al}}$	$96872 \pm 883$	$42179 \pm 884$
$\Delta N_{\text{LiF}}$	$333397 \pm 823$	$31826 \pm 873$
$R_{\text{PE/PE+Al}}$	$1.16 \pm 0.01$	$1.06 \pm 0.03$



(a) Layer 1:  $E_{\text{mean}} \in [5, 20]$  MeV.



(b) Layer 2:  $E_{\text{mean}} \in [20, 150]$  MeV.

**Figure 8.** Flux rate of neutron-like events detected in the experiment at DCPT.

25 meV to 600 MeV. The ratio of the excess signals below PE and PE+Al converters together with the energy deposition spectra of recoiled protons provide means of neutron spectrum assessment. Presented Allpix Squared implementation of a two-layer Timepix3 device is validated against the measured responses. We have outlined data analysis in a radiation field of unknown composition determining thermal and fast neutron flux rates time resolved.

While we have presented the detector characterization in the fast neutron beam at perpendicular impact, the detector response has been determined at different angles covering the entire solid angle range. Finding features indicating the neutron impact angles (e.g., the asymmetry of the excess responses of the layers) will be paramount for precise determination of the absolute fast neutron flux. Furthermore, assessment of the hardness of the (fast) neutron spectrum and the consecutive selection of efficiency was done manually. Future work will focus on utilizing presented data (e.g., the acquired recoil proton spectra) as a response matrix for spectrum unfolding. Moreover, the measured data sets will be able to serve as ground truth for machine learning approaches.

## Acknowledgments

The authors acknowledge funding from the Czech Science Foundation (Research Project GM23-04869M). We thank Yesid Mora for his valuable contributions to the PCB design. We are grateful for the support of the PS/SPS coordinators, operators, technicians.

## References

- [1] T. Holý et al., *Proposal to measure spectral characteristics and composition of radiation in ATLAS by MEDIPIX2-USB Devices*, ATLAS Internal Note (2006), p. 1–12.
- [2] C. Leroy, S. Pospíšil, M. Suk and Z. Vykydal, *Proposal to Measure Radiation Field Characteristics, Luminosity and induced Radioactivity in ATLAS with TIMEPIX Devices*, ATL-R-MA-0001 (2014), p. 1–10.
- [3] M. Campbell et al., *Analysis of the Radiation Field in ATLAS Using 2008 2011 Data from the ATLAS-MPX Network*, ATL-GEN-PUB-2013-001, CERN, Geneva (2013).
- [4] B. Bergmann, T. Billoud, C. Leroy and S. Pospíšil, *Characterization of the Radiation Field in the ATLAS Experiment With Timepix Detectors*, *IEEE Trans. Nucl. Sci.* **66** (2019) 1861.
- [5] M. Campbell et al., *Induced radioactivity in ATLAS cavern measured by MPX detector network*, 2019 *JINST* **14** P03010.
- [6] ATLAS collaboration, *Luminosity determination in pp collisions at  $\sqrt{s} = 8$  TeV using the ATLAS detector at the LHC*, *Eur. Phys. J. C* **76** (2016) 653 [[arXiv:1608.03953](https://arxiv.org/abs/1608.03953)].
- [7] A. Sopczak et al., *Precision Luminosity of LHC Proton–Proton Collisions at 13 TeV Using Hit Counting With TPX Pixel Devices*, *IEEE Trans. Nucl. Sci.* **64** (2017) 915 [[arXiv:1702.00711](https://arxiv.org/abs/1702.00711)].
- [8] ATLAS collaboration, *Radiation Field Study in ATLAS: Timepix measurements vs Geant4 simulations*, ATL-SOFT-PROC-2021-019, CERN, Geneva (2021).
- [9] P. Burian et al., *Timepix3 detector network at ATLAS experiment*, 2018 *JINST* **13** C11024.
- [10] B. Bergmann et al., *Relative luminosity measurement with Timepix3 in ATLAS*, 2020 *JINST* **15** C01039.
- [11] B. Bergmann et al., *Timepix3 as solid-state time-projection chamber in particle and nuclear physics*, *PoS ICHEP2020* (2021) 720.
- [12] T. Poikela et al., *Timepix3: a 65K channel hybrid pixel readout chip with simultaneous ToA/ToT and sparse readout*, 2014 *JINST* **9** C05013.
- [13] <https://medipix.web.cern.ch/>, accessed on 19 September 2023.
- [14] J. Jakubek, *Precise energy calibration of pixel detector working in time-over-threshold mode*, *Nucl. Instrum. Meth. A* **633** (2011) S262.
- [15] P. Burian et al., *Katherine: Ethernet Embedded Readout Interface for Timepix3*, 2017 *JINST* **12** C11001.
- [16] Z. Vykydal et al., *Characterization of the graphite pile as a source of thermal neutrons*, *Radiat. Phys. Chem.* **116** (2015) 65.
- [17] Z. Vykydal and M. Kralak, *Characterisation of the graphite moderated thermal neutron field at CMI*, *Radiat. Prot. Dosimetry* **180** (2018) 51.
- [18] P.W. Lisowski and K.F. Schoenberg, *The Los Alamos Neutron Science Center*, *Nucl. Instrum. Meth. A* **562** (2006) 910.
- [19] n\_TOF collaboration, *Status and outlook of the neutron time-of-flight facility n\_TOF at CERN*, *Nucl. Instrum. Meth. B* **261** (2007) 925.
- [20] C. Guerrero et al., *Performance of the neutron time-of-flight facility n\_TOF at CERN*, *Eur. Phys. J. A* **49** (2013) 27.
- [21] B. Bergmann et al., *Time-of-flight measurement of fast neutrons with Timepix detectors*, 2014 *JINST* **9** C05048.

- [22] ATLAS collaboration, *Particle tracking and radiation field characterization with Timepix3 in ATLAS*, *Nucl. Instrum. Meth. A* **978** (2020) 164401.
- [23] P. Mánek et al., *Improved algorithms for determination of particle directions with Timepix3*, *2022 JINST* **17** C01062 [[arXiv:2111.00624](#)].
- [24] B. Bergmann et al., *3D track reconstruction capability of a silicon hybrid active pixel detector*, *Eur. Phys. J. C* **77** (2017) 421.
- [25] B. Bergmann, P. Burian, P. Mánek and S. Pospíšil, *3D reconstruction of particle tracks in a 2 mm thick CdTe hybrid pixel detector*, *Eur. Phys. J. C* **79** (2019) 165.
- [26] B. Bergmann et al., *ATLAS-TPX: a two-layer pixel detector setup for neutron detection and radiation field characterization*, *2016 JINST* **11** P10002.
- [27] D. Vavrik et al., *Position sensitive detection of neutrons in high radiation background field*, *Rev. Sci. Instrum.* **85** (2014) 013304.
- [28] S. Spannagel et al., *Allpix<sup>2</sup>: A Modular Simulation Framework for Silicon Detectors*, *Nucl. Instrum. Meth. A* **901** (2018) 164 [[arXiv:1806.05813](#)].
- [29] A.B. Alpat, A. Coban, H. Kaya and G. Bartolini, *MRADSIM-Converter: A new software for STEP to GDML conversion*, [arXiv:2305.00902](#) [[DOI:10.1016/j.cpc.2023.108688](#)].